

Flow and dispersion in an urban cubical cavity

Young-Hee Ryu, Jong-Jin Baik*

School of Earth and Environmental Sciences, Seoul National University, Seoul 151-742, Republic of Korea

ARTICLE INFO

Article history:

Received 29 July 2008

Received in revised form

19 November 2008

Accepted 8 December 2008

Keywords:

Reynolds-averaged Navier–Stokes equations

(RANS) model

Flow and dispersion

Urban cubical cavity

End-walls

Time constant

ABSTRACT

Flow and dispersion in an urban cubical cavity are numerically investigated using a Reynolds-averaged Navier–Stokes equations (RANS) model with the renormalization group (RNG) $k-\varepsilon$ turbulence closure model. The urban cubical cavity is surrounded by flank walls that are parallel to the streamwise direction, called end-walls, as well as upstream and downstream walls. A primary vortex and secondary vortices including end-wall vortices are formed in the cavity. Because of the end-wall drag effect, the averaged mean-flow kinetic energy in the cavity is smaller than that in an urban street canyon that is open in the along-canyon direction. A trajectory analysis shows that the end-wall vortices cause fluid particles to move in the spanwise direction, indicating that flow in the cavity is essentially three-dimensional. The iso-surfaces of the Okubo–Weiss criterion capture cavity vortices well. The pollutant concentration is high near the bottom of the upstream side in the case of continuous pollutant emission, whereas it is high near the center of the primary vortex in the case of instantaneous pollutant emission. To get some insight into the degree of pollutant escape from the cavity according to various meteorological factors, extensive numerical experiments with different ambient wind speeds and directions, inflow turbulence intensities, and cavity-bottom heating intensities are performed. For each experiment, we calculate the time constant, which is defined as the time taken for the pollutant concentration to decrease to e^{-1} of its initial value. The time constant decreases substantially with increasing ambient wind speed, and tends to decrease with increasing inflow turbulence intensity and cavity-bottom heating intensity. The time constant increases as the ambient wind direction becomes oblique. High ambient wind speed is found to be the most crucial factor for ventilating the cavity, thus improving air quality in an urban cubical cavity.

© 2008 Elsevier Ltd. All rights reserved.

1. Introduction

Flows in a three-dimensional cavity have received much attention in fluid mechanics because many interesting phenomena such as eddies, secondary flows, complex three-dimensional patterns, chaotic particle motions, instabilities, transition, and turbulence can occur therein (Shankar and Deshpande, 2000). Moreover, a cavity is a fundamental structure and is ideal for understanding three-dimensional flows. Most of cavity flows that have been studied in fluid mechanics are lid-driven cavity flows. The lid-driven cavity flow means that the circulating flow in a cavity is driven by shear stress that is induced by a lid imposed at the top of the cavity (Koseff and Street, 1984).

One of the pioneer investigations into lid-driven cavity flows is the fluid experiment conducted by Koseff and Street (1984) (Shankar and Deshpande, 2000). Their work clearly indicates that cavity flows are inherently three-dimensional and hence two-dimensional

studies of cavity flows can be misleading (Shankar and Deshpande, 2000). Flows in three dimensions are quite different from those in two dimensions. Because a cavity has lateral walls that are parallel to the streamwise direction, called end-walls, significant longitudinal or spanwise motions appear in the cavity, so that a three-dimensional analysis should be considered. There are a number of fluid experimental and numerical modeling studies of three-dimensional lid-driven cavity flows (Koseff and Street, 1984; Prasad and Koseff, 1989; Jordan and Ragab, 1994; Chiang et al., 1996; Migeon et al., 2003; Tsorng et al., 2006). One of the most significant effects of the end-walls is to form end-wall vortices that do not appear in two dimensions.

This study is concerned with flow and dispersion in an urban cavity. The urban cavity flow resembles the lid-driven cavity flow, but the flow therein is driven by wind shear stress just above the top of the cavity, generally building-roof height. Although a perfectly enclosed urban cavity is relatively hard to find in a real urban area, there are a number of structures that form urban cavities; for example, plazas, castles, and gardens enclosed by fences or trees. Due to the surrounding walls including end-walls, the urban cavity has poor air qualities in contaminated conditions,

* Corresponding author. Tel.: +82 2 880 6990; fax: +82 2 883 4972.

E-mail address: jjbaik@snu.ac.kr (J.-J. Baik).

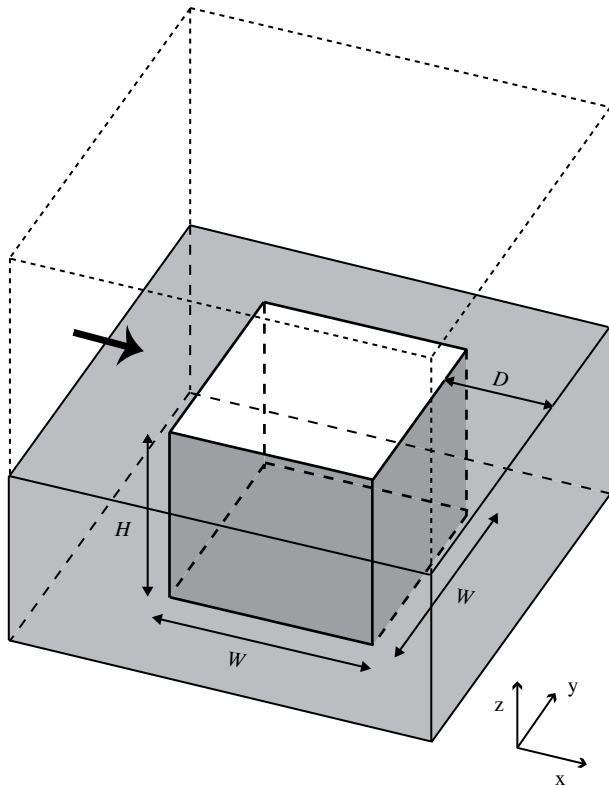


Fig. 1. Computational domain and cavity configuration. H is the cavity height and W is the cavity width. The thick arrow denotes the ambient wind.

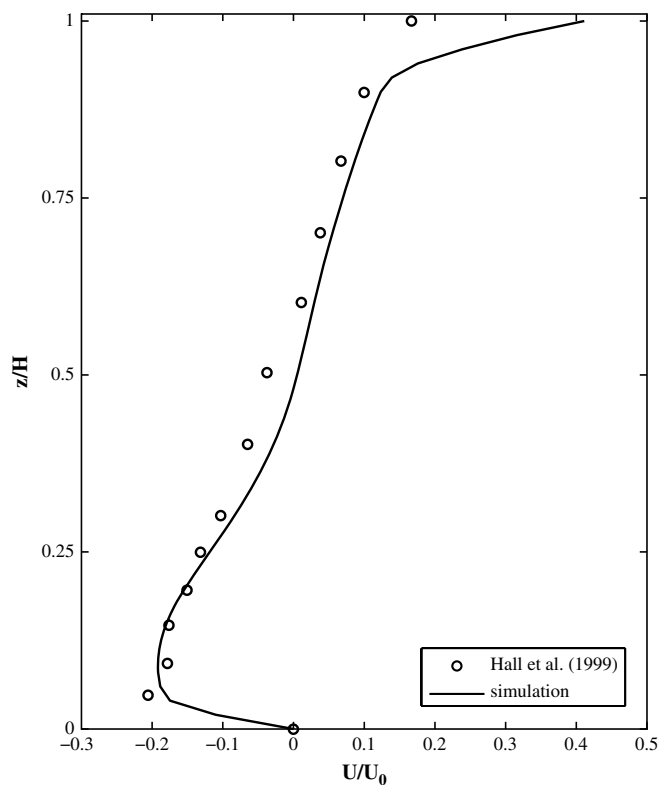


Fig. 2. Vertical profile of normalized horizontal velocity at the center of the cubical cavity in the wind tunnel experiment of Hall et al. (1999) and the present numerical simulation at $t = 1$ h. H is the cavity height and U_0 is the ambient wind speed at $z = H$.

as demonstrated in a wind tunnel experiment by Hall et al. (1999). Hence, the cavity is an ideal structure for rigorously examining conditions for creating better ventilation in the cavity. A useful quantity to measure the degree of ventilation of a scalar (say, pollutants) in an urban cavity is the time constant. The time constant is defined as the time taken for the pollutant

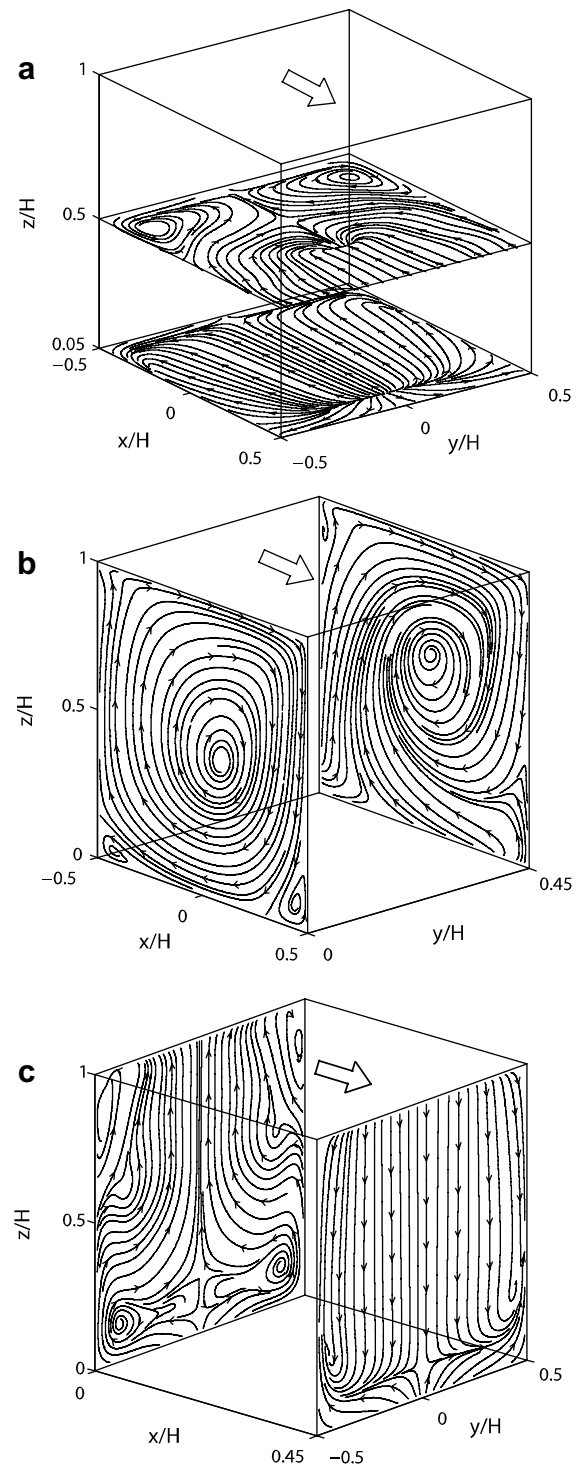


Fig. 3. Streamline fields at $t = 1$ h at (a) $z/H = 0.05$ and 0.5 , (b) $y/H = 0$ and 0.45 , and (c) $x/H = 0$ and 0.45 in the control experiment. Arrows indicate the ambient wind. Note that cavity sizes in the x - and y -direction are not the same except for (a) for presentation purpose.

concentration to decrease to e^{-1} of its initial value (Lee and Park, 1994). Meteorology and cavity geometry can affect the time constant.

In this study, flow and dispersion in an urban cubical cavity are numerically investigated using a computational fluid dynamics (CFD) model. A study of urban cubical cavity flow can be a prototype for studies of flows in urban cavities having complex shapes. First, the three-dimensional characteristics of flow in an urban cubical cavity are identified through streamline and trajectory analyses. Second, the features of dispersion in the cubical cavity are examined through concentration field analyses for both continuous and instantaneous pollutant emission cases. Third, the time constant is calculated to examine how the pollutant concentration in the cubical cavity varies with changes in various meteorological factors. Reasons for the variation are explained using the mean-flow kinetic energy and turbulent kinetic energy. Meteorological factors considered are ambient wind speed, ambient wind direction, inflow turbulence intensity, and cavity-bottom heating by solar radiation. The experimental setup is described in Section 2 and the model is validated in Section 3. Results and discussion are given in Section 4. Summary and conclusions follow in Section 5.

2. Experimental setup

The CFD model used in this study is the Reynolds-averaged Navier–Stokes equations (RANS) model with the renormalization

group (RNG) k - ε turbulence closure model developed by Kim and Baik (2004). The numerical method for solving the governing equations is described in Baik et al. (2003). The computational domain and cavity configuration are shown in Fig. 1. The width and height of the cubical cavity are set equal to 20 m. The grid interval in the cavity and up to four grids outside each cavity wall is uniform with 0.4 m. The grid interval outside the four grids is non-uniform with an expansion ratio of 1.1 and the largest grid size is 2.02 m. The computational domain size is 58.88 m in both x - and y -direction and 51.57 m in the z -direction. D in Fig. 1 is 19.44 m. The time step is 0.05 s. The numerical model is integrated for 1 h in all experiments except for an experiment with an ambient wind speed of 1 m s^{-1} (90 min).

The inflow boundary conditions are given by

$$U_0 = U_r \cos \theta, \quad (1)$$

$$V_0 = U_r \sin \theta, \quad (2)$$

$$W_0 = 0, \quad (3)$$

$$k_0 = \frac{1}{2} \alpha (U_0^2 + V_0^2), \quad (4)$$

$$\varepsilon_0 = \frac{C_\mu^{3/4} k_0^{3/2}}{\kappa Z_r}, \quad (5)$$

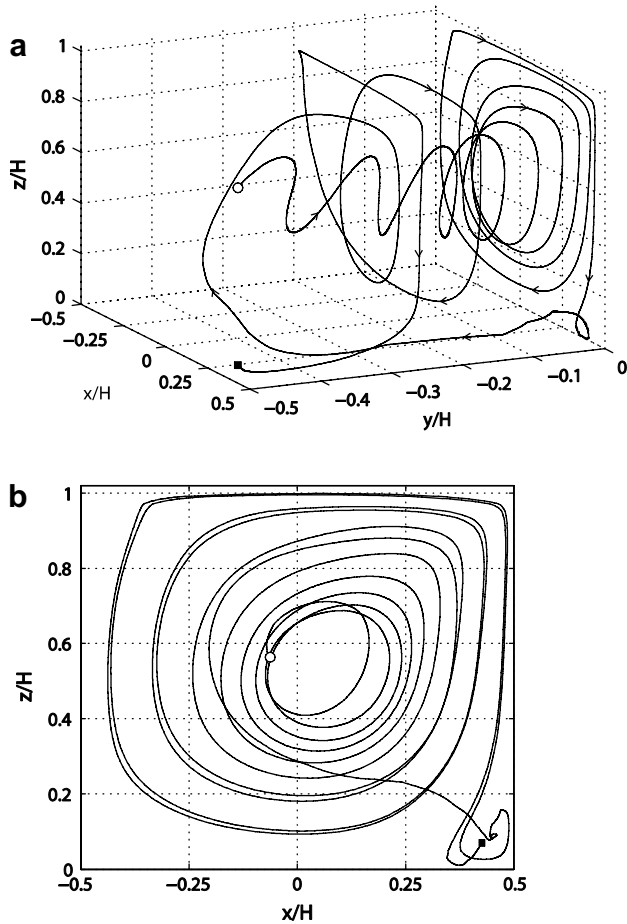


Fig. 4. (a) Trajectory of a particle released at a location of $(-0.068H, -0.38H, 0.56H)$ at $t = 30$ min. The terminal point location is $(0.43H, -0.5H, 0.07H)$ at $t = 46$ min. (b) Projection of the particle trajectory on the x - z plane. The initial point and terminal point are denoted by an unfilled circle and a filled square, respectively.

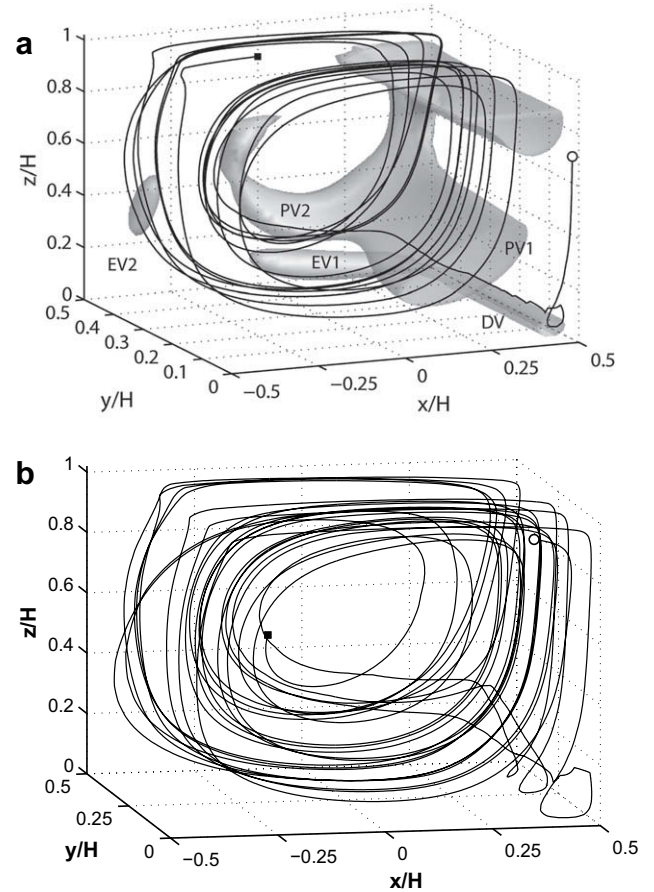


Fig. 5. (a) Trajectory of a particle released at a location of $(0.49H, 0.01H, 0.71H)$ at $t = 30$ min. The gray surfaces show the iso-surfaces of the Okubo-Weiss criterion $Q = 0.016 \text{ s}^{-2}$ at $t = 1$ h. The meanings of symbols EV1, EV2, DV, PV1, and PV2 are explained in the text. (b) Trajectory of a particle released at a location of $(0.35H, 0.01H, 0.95H)$ at $t = 30$ min. The initial point and terminal point are denoted by an unfilled circle and a filled square, respectively.

where U_0 , V_0 , and W_0 are the components of the ambient wind velocity (its speed is denoted by U_f) in the x -, y -, and z -direction, respectively, and k_0 and ε_0 are the inflow turbulent kinetic energy (TKE) and its dissipation rate, respectively. θ is the ambient wind direction (measured counterclockwise from the positive x -axis), C_μ is an empirical constant ($=0.0845$), and κ is the von Karman constant ($=0.4$). The zero-gradient condition is applied at the outflow and upper boundaries and the wall boundary conditions suggested by Versteeg and Malalasekera (1995) are employed. α is a parameter that represents a ratio of the inflow TKE to the kinetic energy of the ambient wind. The inflow dissipation rate is specified as a value at a certain height ($z_f = 30$ m). In the control experiment, the ambient wind blows parallel to the x -axis ($\theta = 0^\circ$), $U_f = 5$ m s $^{-1}$, $\alpha = 0.05$, and there is no cavity-bottom heating. The Reynolds number ($Re = U_f H / \nu$, where H is the cavity height and ν is the kinematic viscosity of air) in the control experiment is 6.85×10^6 . The origin of the coordinate system is located at the center of the bottom of the cubical cavity.

Two different cases of passive pollutant emission are considered in this study. In the first case, pollutants are continuously emitted with an emission rate of 50 ppb s $^{-1}$ at all grid points of the lowest model level ($z = 0.2$ m) of the cavity starting from $t = 30$ min. In the second, the initial pollutant concentration is set to be uniform everywhere in the cavity with 50 ppb at $t = 30$ min and no emission of pollutants is allowed thereafter. Thus, the averaged pollutant concentration in the cavity decreases with time, enabling us to calculate the time constant.

3. Model validation

The vertical profile of normalized horizontal velocity at the center of the cubical cavity obtained by our CFD model is compared with the wind tunnel experimental data of Hall et al. (1999) (Fig. 2).

The numerical simulation result is at $t = 1$ h. Since the flow in the control experiment is in a quasi-steady state after $t = 30$ min, the velocity profile at $t = 1$ h can be compared with the time-averaged velocity profile in the wind tunnel experiment. The horizontal velocity is normalized by the ambient wind speed at the top of the cavity in both cases. A discrepancy is observed near the top of the cavity. The inflow boundary condition is to some extent responsible for this discrepancy because the inflow boundary flow is set up as a log profile in Hall et al. (1999) but is constant with height in the numerical simulation. However, except for near the top of the cavity, the vertical profiles of the normalized horizontal velocity are very similar to each other, indicating that the present CFD model can be reliably utilized in the simulation of cubical cavity flow.

4. Results and discussion

4.1. Flow and dispersion characteristics

The three-dimensional characteristics of flow in the cubical cavity in the control experiment are examined first. An urban street canyon experiment (meaning in this study that the canyon space is open in the y -direction, not bounded by buildings in that direction) is also performed to compare flow fields. The street canyon experiment is carried out in exactly the same way as the cavity experiment, but without the end-walls. Fig. 3 shows streamline fields at $t = 1$ h at different planes of $z/H = 0.05, 0.5$, $y/H = 0, 0.45$, and $x/H = 0, 0.45$. A primary vortex is produced in the cavity and upstream and downstream vortices appear at the bottom corners of the cavity (Fig. 3b). These flow patterns in the x - z plane are similar to those in an urban street canyon studied by Kim and Baik (2003). However, flow patterns represented in the x - y and y - z planes (Fig. 3a and c) are quite different from those in a street canyon because of the existence of end-walls. For example, end-wall

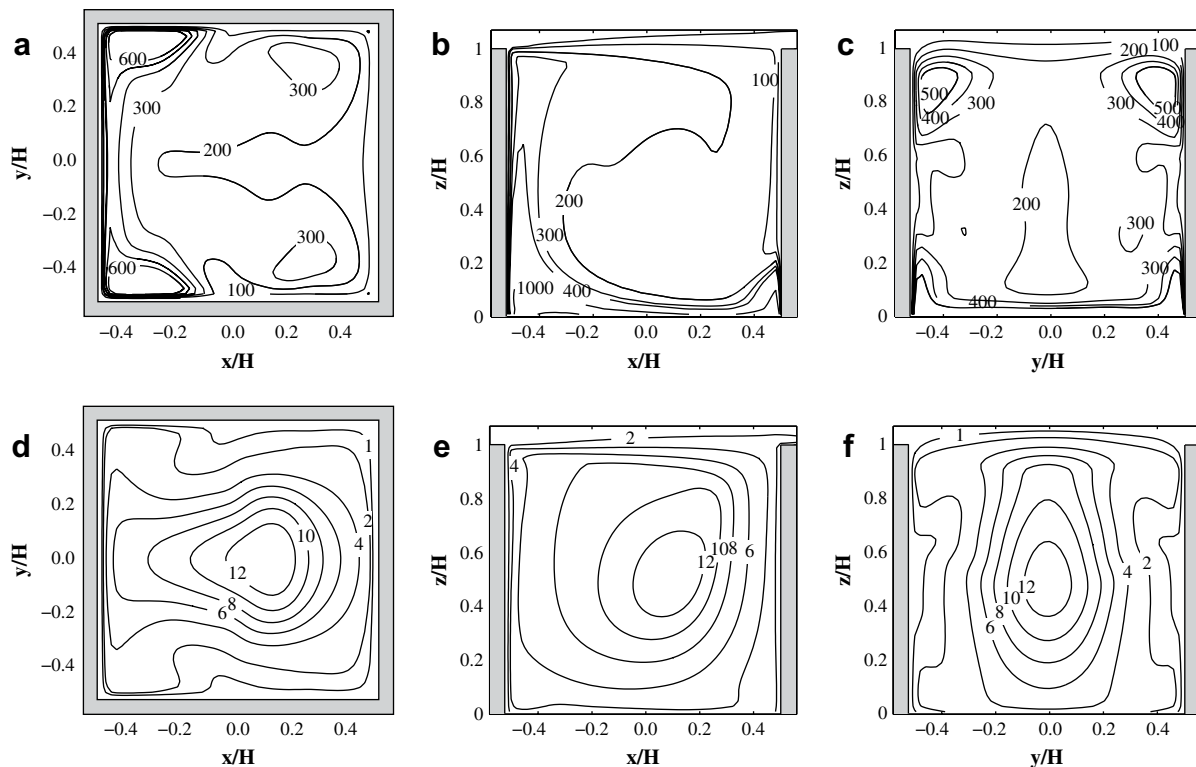


Fig. 6. Pollutant concentration fields at $t = 1$ h. (a), (b), and (c) are for the case of continuous pollutant emission and (d), (e), and (f) are for the case of instantaneous pollutant emission. (a) and (d) are at $z/H = 0.5$, (b) and (e) are at $y/H = 0$, and (c) and (f) are at $x/H = 0$. The unit is ppb.

vortices that are located at the corners in the x - y plane ($z/H = 0.5$) and at the bottom corners in the y - z plane ($x/H = 0$) are produced in the cavity. The end-wall vortex is produced as a result of the complex interaction of the spanwise pressure gradient, radial pressure gradient, and centrifugal force and the no-slip velocity boundary condition (Freitas and Street, 1988). When the ambient wind direction is perpendicular to the along-canyon direction and there is no street-bottom heating, the street canyon flow is essentially two-dimensional and there is very little variation of flow in the along-canyon direction (not shown).

The mean-flow kinetic energy (MKE) averaged over the cavity and street canyon is calculated. The averaged MKE in the cavity experiment is 30.2% of the averaged MKE in the street canyon experiment. The effect of end-walls on the flow velocity in the cavity was studied by Prasad and Koseff (1989). They found that the flow velocity in the cavity is reduced as the fractional area of end-walls increases. The smaller averaged MKE in the cavity experiment is of course due to the drag effect of the end-walls (Prasad and Koseff, 1989).

Fig. 4 shows the trajectory of a particle released at a location of $(-0.068H, -0.38H, 0.56H)$ at $t = 30$ min. The particle trajectory is simple but shows the important characteristics of three-dimensional cavity flows clearly. A particle departing from the core region of the primary vortex moves toward the mid-plane ($y/H = 0$) with a spiral motion. It takes about 8 min for the particle to arrive at the mid-plane, meaning that the spiral motion is quite slow and winds are very weak in the core region. Then, the particle rotates several times at the mid-plane for about 2 min, with outward rotations from the center of the mid-plane. After the particle escapes from the primary vortex, it is entrained into the downstream vortex and moves toward the end-wall ($y/H = -0.5$). It takes about 2 min in doing so. Then, the particle is lifted up to the primary vortex under the influence of the rotational flow by the end-wall vortex. The rotational flow is also seen by the streamline field at $x/H = 0$ in Fig. 3c. Due to the end-wall vortex, the particle can maintain its movement in the spanwise direction by associating with the primary vortex again. In the street canyon experiment, however, the spanwise motion resulting from the downstream vortex does not terminate. The particle motion represented by the trajectory is similar to that of Chiang et al. (1996), although in their study the Reynolds number is much smaller ($Re = 1500$) and the cavity shape is not cubical but longer in the y -direction than in the x - and z -direction. However, particle trajectories in their study are quite simple compared with our results. As shown in Fig. 4b, a two-dimensional analysis is not adequate to describe the flow in the cavity, for example, longitudinal motions along the y -direction. The cavity flow is essentially three-dimensional.

Fig. 5 shows the trajectory of a particle released at a location of $(0.49H, 0.01H, 0.71H)$ at $t = 30$ min and the iso-surfaces of the Okubo–Weiss criterion $Q = 0.016 \text{ s}^{-2}$ at $t = 1$ h (Fig. 5a) and also the trajectory of a particle released at a location of $(0.35H, 0.01H, 0.95H)$ at $t = 30$ min (Fig. 5b). The Okubo–Weiss criterion Q (Okubo, 1970; Weiss, 1991) is defined as follows.

$$Q = \frac{1}{2}(|\boldsymbol{\Omega}|^2 - |\mathbf{S}|^2), \quad (6)$$

where

$$\boldsymbol{\Omega} = \frac{1}{2}[\nabla \mathbf{u} - (\nabla \mathbf{u})^T], \mathbf{S} = \frac{1}{2}[\nabla \mathbf{u} + (\nabla \mathbf{u})^T]. \quad (7)$$

Here, $|\cdot|$ denotes the Euclidean matrix norm (Haller and Sapsis, 2008), \mathbf{u} is the velocity, $\boldsymbol{\Omega}$ is the vorticity tensor, and \mathbf{S} is the strain rate tensor. The superscript T denotes the transpose. According to the definition of Q , an iso-surface of positive Q value represents

a vorticity-dominant region rather than a strain rate-dominant region.

As seen in Fig. 5a, the closed iso-surfaces of Q correspond well to the downstream vortex (DV) and end-wall vortices (EV1 and EV2) as well as the primary vortex (PV1 and PV2). Here, two end-wall vortices appear. One is located near $y/H = 0.5$ along the x -axis (EV1) and the other is located near the corner of the cavity along the z -

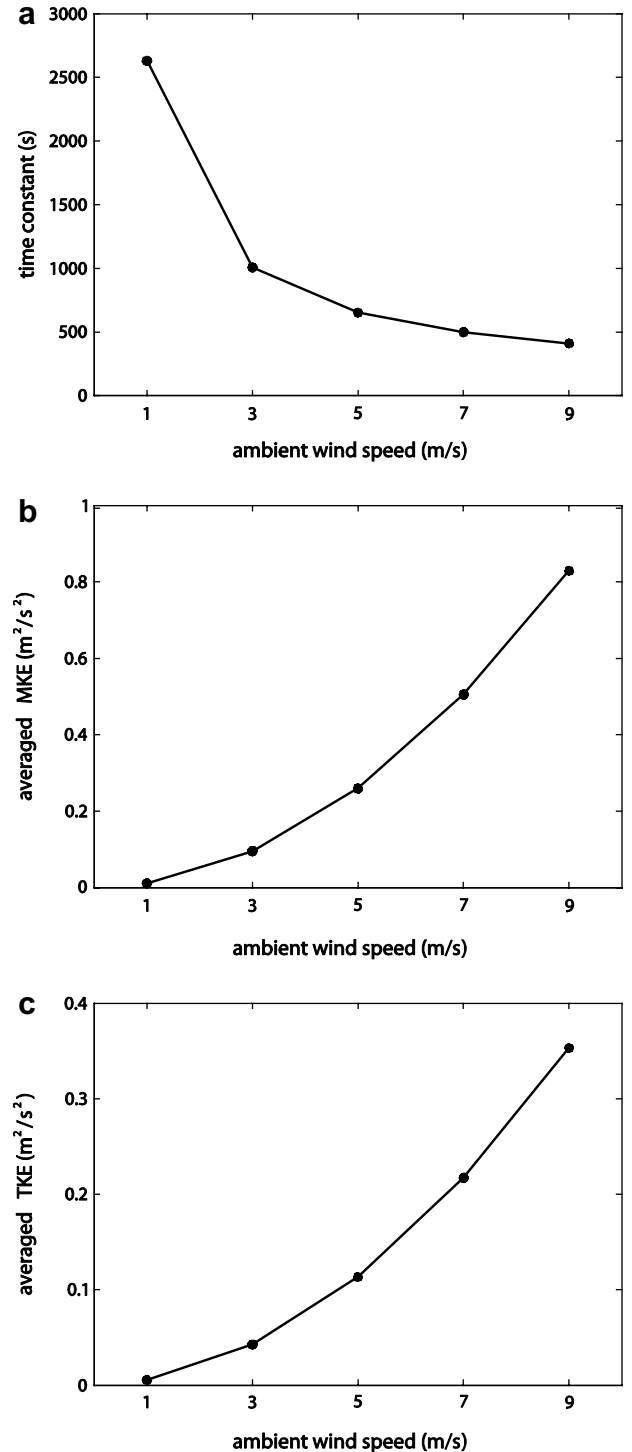


Fig. 7. Variations of (a) time constant (b) averaged mean-flow kinetic energy (MKE), and (c) averaged turbulent kinetic energy (TKE) with the ambient wind speed. The average is taken over the urban cubical cavity at $t = 1$ h.

axis (EV2). The primary vortex is represented by the iso-surface of Q and we designate the main primary vortex as PV1 and the other as PV2. PV1 is consistent with the primary vortex in Fig. 3b (streamline field at $y/H = 0$). PV1 also resembles a primary vortex in the street canyon experiment that does not have end-walls. PV2 appears near the end-wall and is strongly influenced by the drag of the end-wall, so that its shape is curly as shown in the streamline field at $y/H = 0.45$ (Fig. 3b). Similar to Fig. 4a, a particle is entrained into the downstream vortex (DV) from the primary vortex (PV1). Then, the particle is lifted up to the primary vortex (PV2) near $y/H = 0.5$ due to the end-wall vortex (EV1). After the particle rotates while wrapping around PV2, it associates with PV1. Because of the rotational flow by the end-wall vortex (EV2), the particle is drawn into the end-wall. This is also seen in the streamline field at $z/H = 0.5$ in Fig. 3a. Then, the particle becomes influenced by the primary vortex (PV2) again. Consequently, the trajectory near the end-wall that is concentrated in a certain track is due to various vortices. One can see that the particle does not enter or stay inside

the region of the iso-surface of Q except for the downstream vortex, although the particle approaches the vortices. In other words, the particle is unlikely to enter a vorticity-dominant region. As shown in Fig. 4a, it is possible for a particle to be entrained into the primary vortex, but many other particles wrap around the vortices.

Fig. 5b shows a typical trajectory in the cavity, exhibiting a trajectory clustering in the primary vortex region. The trajectory is also strongly influenced by various vortices. In particular, the end-wall vortices are critical in the three-dimensional cavity. It is worth pointing out that one of the most important differences between cavity flow and canyon flow is the outward/inward flow from/to the core of the primary vortex. Most of the particles in the cavity escape eventually from the core of the primary vortex, whereas the analysis showed that particles in a primary vortex of the canyon stay there and rarely escape. As shown in Fig. 5b, there is no inward flow that causes a particle to stay in the primary vortex.

Fig. 6 shows pollutant concentration fields at $z/H = 0.5$, $y/H = 0$, and $x/H = 0$ at $t = 1$ h in the case of continuous emission and that of instantaneous emission. In the case of continuous emission, the highest pollutant concentration appears near the bottom of the upstream side (Fig. 6b). This is due to the advection of pollutants by upstreamward flow in the lower region of the cavity (see Fig. 3a). The high concentration of pollutants appears in regions associated with the various vortices; for example, the end-wall vortex (EV2) in Fig. 6a, the upstream vortex (UV) and downstream vortex (DV) in

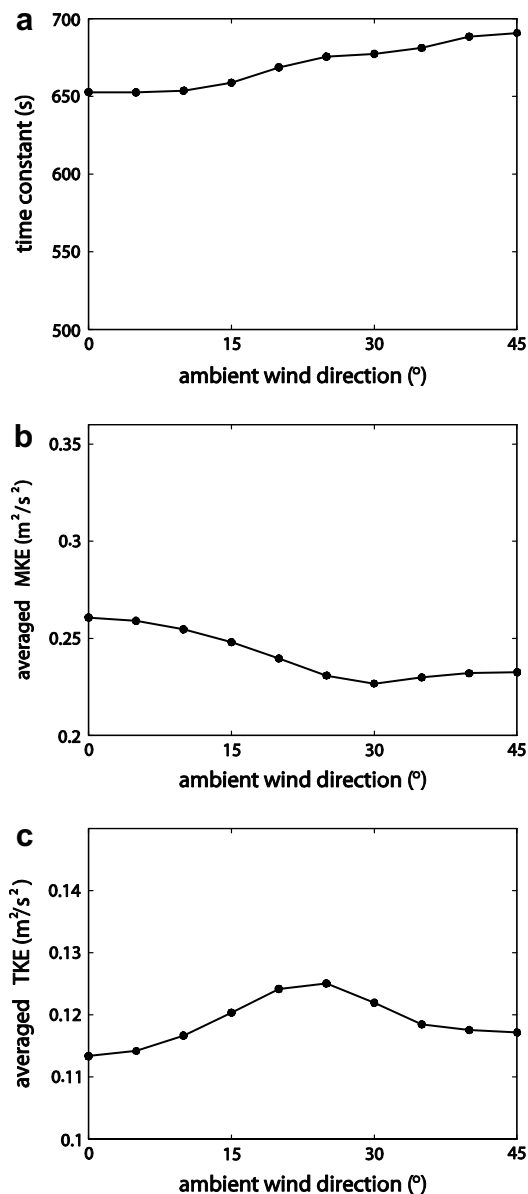


Fig. 8. The same as in Fig. 7 except for the ambient wind direction.

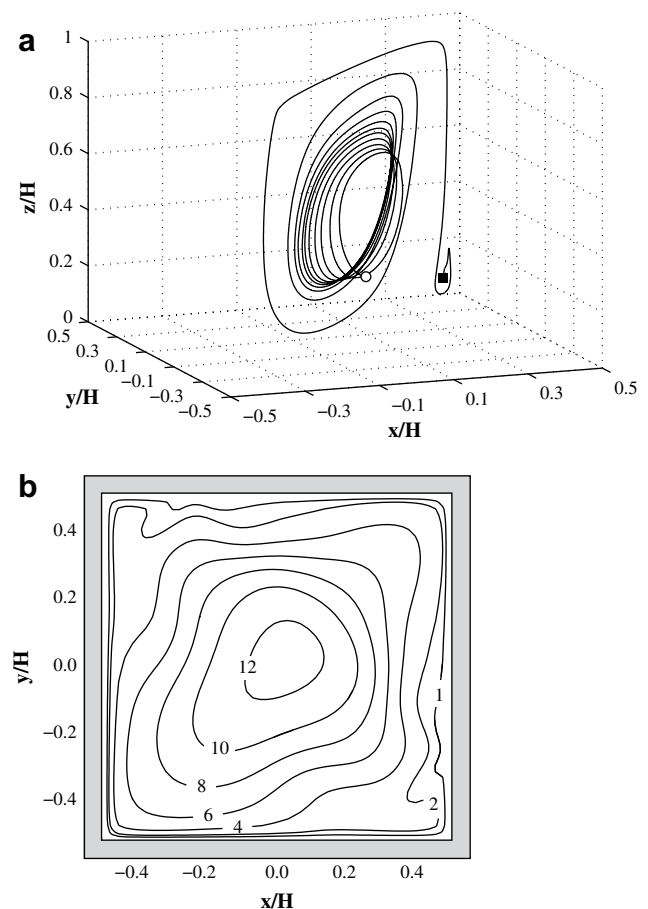


Fig. 9. (a) Trajectory of a particle released at a location of $(-0.01H, -0.17H, 0.29H)$ at $t = 30$ min in the experiment of an ambient wind direction of 45° . The initial point and terminal point are denoted by an unfilled circle and a filled square, respectively. (b) Pollutant concentration field at $z/H = 0.5$ at $t = 1$ h in the experiment of an ambient wind direction of 45° . The unit is ppb.

Fig. 6b, and the end-wall vortex (EV1) in Fig. 6c. Unlike in the case of continuous emission, the highest pollutant concentration in the case of instantaneous emission appears near the center of the cavity (Fig. 6d–f). As shown in Fig. 4a, a particle inside the primary vortex requires quite a long time to escape from the vortex core. This is a crucial factor in determining pollutant concentration in the cavity. Although the impact of secondary vortices on pollutant concentration is relatively small compared with that in the case of continuous emission, the pollutant concentration is still high in regions where secondary vortices are located.

4.2. Time constant

In this subsection, time constant results are presented and discussed. Numerical experiments are performed by systematically changing the ambient wind speed, ambient wind direction, inflow turbulence intensity, and cavity-bottom heating intensity. The pollutant concentration is set to be uniform in the cavity at

$t = 30$ min and pollutant emission is not allowed thereafter. As time progresses, the cavity-averaged pollutant concentration decreases and eventually reaches a value of e^{-1} times the initial pollutant concentration at $t = 30$ min. Hence, the time constant can be determined for a particular numerical experiment.

Fig. 7 shows the variation of the time constant with the ambient wind speed. Also shown are the variations of the mean-flow kinetic energy (MKE) and turbulent kinetic energy (TKE) averaged over the cavity at $t = 1$ h. The ambient wind speeds considered are 1, 3, 5 (control experiment), 7, and 9 m s^{-1} . The Reynolds number varies from 1.37×10^6 to 1.23×10^7 as U_r varies from 1 to 9 m s^{-1} . The time constant in the control experiment is 653 s. As the ambient wind speed increases, the time constant decreases rapidly. That is, pollutants escape more and more rapidly from the cavity with increasing ambient wind speed. The time constant in the experiment with an ambient wind speed of 3 m s^{-1} (1006 s) is 2.6 times smaller than that in the experiment with an ambient wind speed of 1 m s^{-1} (2632 s). A regression equation between the time constant

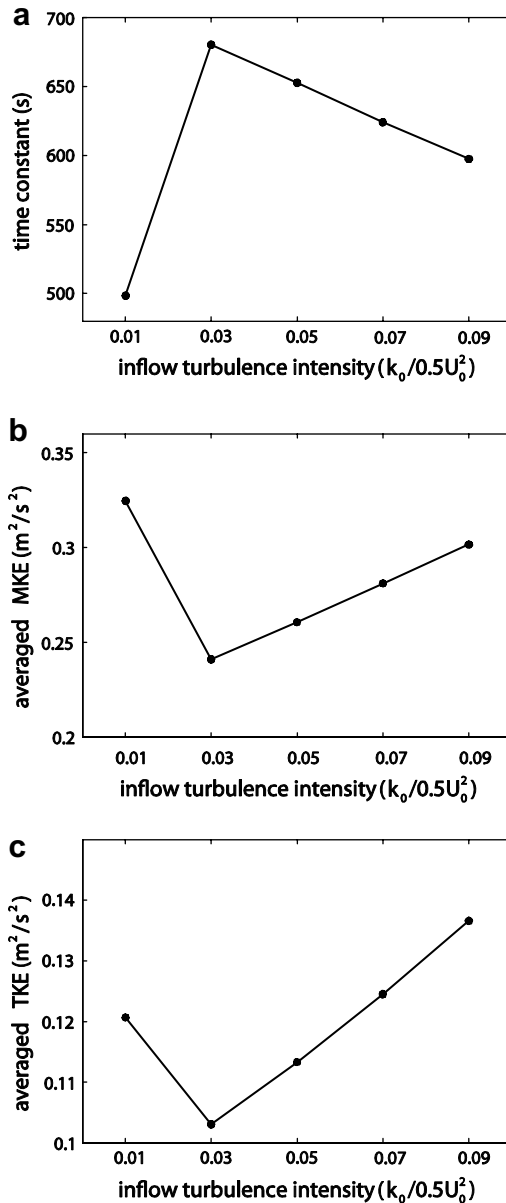


Fig. 10. The same as in Fig. 7 except for the inflow turbulence intensity.

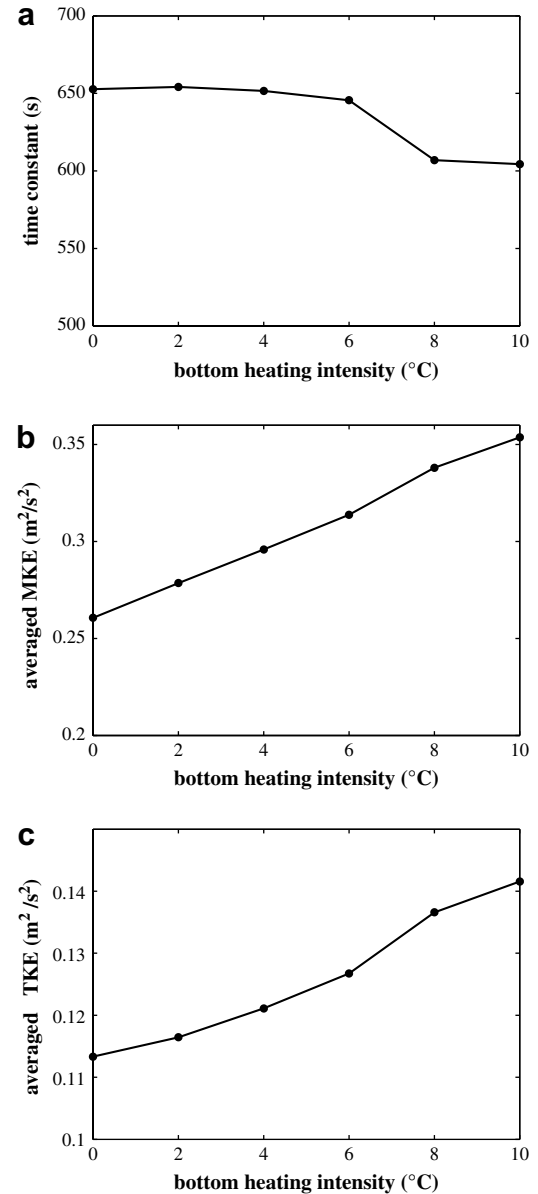


Fig. 11. The same as in Fig. 7 except for the cavity-bottom heating intensity.

(τ) and the ambient wind speed (U_f) based on the simulation data in Fig. 7a is $\tau = 2630U_f^{-0.8631}$ with $R^2 = 0.99$. Note that this regression equation is valid for the cases of $\theta = 0^\circ$. The cavity-averaged MKE and TKE increase as the ambient wind speed increases. This means that mean-flow and turbulence in the cavity strengthen as the ambient wind speed increases. The strengthened mean-flow and turbulence give rise to a rapid escape of pollutants from the cavity. Note that in the control experiment the averaged TKE is 43.5% smaller than the averaged MKE.

Fig. 8 shows the variations of the time constant, averaged MKE, and averaged TKE with the ambient wind direction. The ambient wind direction varies from 0° to 45° in 5° intervals. The time constant tends to increase as the ambient wind direction increases, but the variation of the time constant is very small compared with that of the ambient wind speed. The time constant is 653 s in the experiment of an ambient wind direction of 0° (control experiment) and 691 s in the experiment of an ambient wind direction of 45° .

Fig. 9 shows the trajectory of a particle released at a location of $(-0.01H, -0.17H, 0.29H)$ at $t = 30$ min and pollutant concentration field at $z/H = 0.5$ at $t = 1$ h in the experiment of an ambient wind direction of 45° . The primary vortex is formed at the oblique plane that is parallel to the ambient wind direction. As the ambient wind direction increases from 0° , the plane on which the primary vortex appears tilts toward the ambient wind direction as it does in the experiment of an ambient wind direction of 45° . Therefore, drag due to the four walls makes the mean wind weaken. This explains the decrease of the averaged MKE (Fig. 8b) with increasing ambient wind direction up to $\sim 30^\circ$. Povitsky (2005) showed that the

volume integral of the square of the velocity for an ambient flow direction of 45° is reduced by 10.9% compared with that for an ambient flow direction of 0° . In the present study, the averaged MKE for an ambient wind direction of 45° is reduced by 10.8% compared with the averaged MKE for an ambient wind direction of 0° , showing very good agreement with the result of Povitsky (2005). In Fig. 9b, a high concentration of pollutants spreads over the corners. This is due to the diagonal wind by the tilted primary vortex. The pollutants distributed near the corners are strongly influenced by the walls since the weakened wind due to the drag makes the pollutants more difficult to escape from the corner, consequently increasing the time constant.

Fig. 10 shows the variations of the time constant, averaged MKE, and averaged TKE with the inflow turbulence intensity. The tested ratios [$=\alpha$ in Eq. (4)] are 0.01, 0.03, 0.05 (control experiment), 0.07, and 0.09. The time constant decreases linearly when α is greater than 3% (Fig. 10a). The averaged TKE in Fig. 10c is related to the inflow turbulence intensity, which is proportional to α . As the inflow turbulence intensity increases, turbulent diffusivity near the roof level also increases (Kim and Baik, 2003). Accordingly, downward momentum transfer from the outside of the cavity increases, causing an increase of horizontal velocity at the roof level. Hence, the averaged MKE in the cavity shows a similar pattern to the averaged TKE. Pollutants can escape more easily due to the strengthened MKE and TKE. When the inflow turbulence intensity is equal to 1%, the cavity-averaged MKE and TKE are large and the time constant is small. This weak inflow turbulence intensity produces an unexpected result, since one might expect that the flow weakens with weak inflow turbulence intensity. We

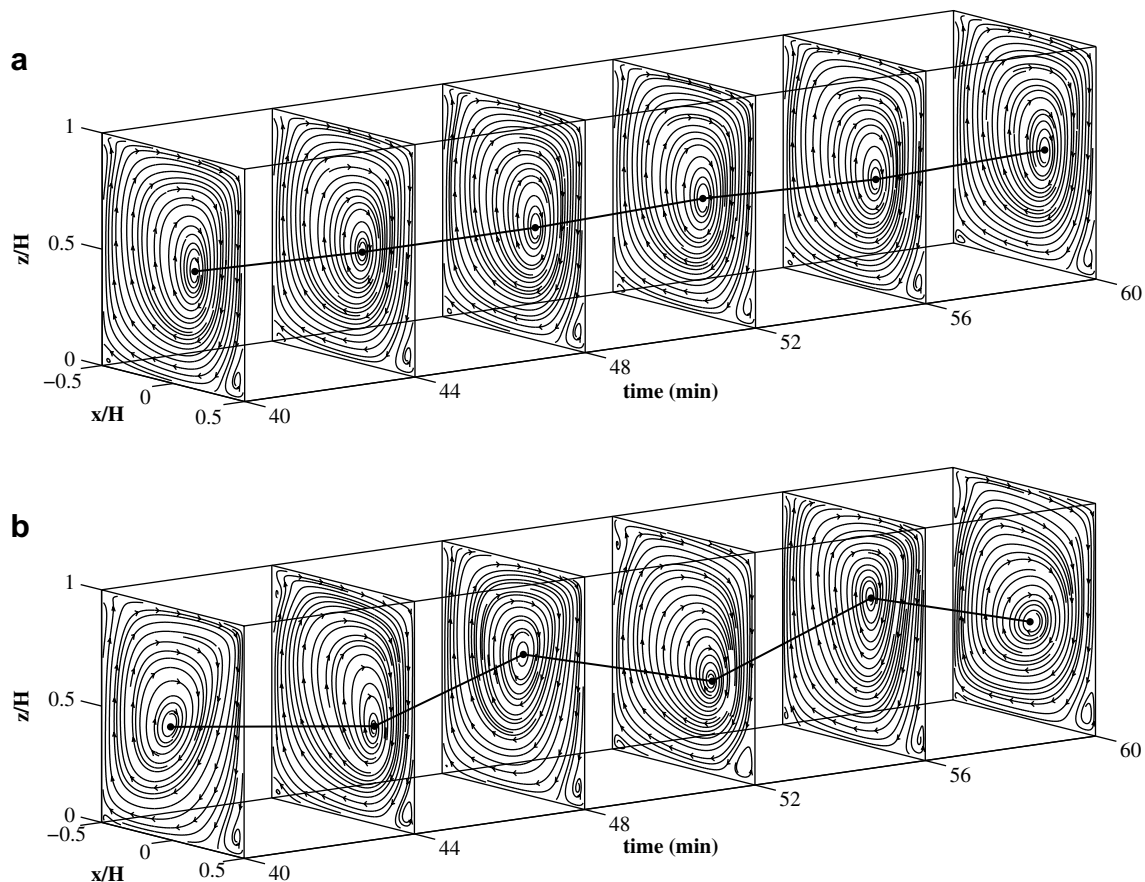


Fig. 12. Time evolution of streamline at $y/H = 0$ in the experiments of $\Delta T =$ (a) 6°C and (b) 10°C . Filled circles indicate centers of the primary vortices at $y/H = 0$ and the primary vortex centers are connected by a solid line.

analyzed the time evolution of streamline field and the time series of cavity-averaged MKE and TKE in the experiment of $\alpha = 1\%$. The results showed that the flow in the experiment of $\alpha = 1\%$ is unsteady unlike flows in the experiments of $\alpha = 3, 5, 7$, and 9% that exhibit quasi-steady states and that the averaged MKE and TKE oscillate in time with large amplitudes. The weak inflow turbulence intensity ($\alpha = 1\%$) makes the flow become unsteady and more turbulent, reducing the time constant. However, at present it is difficult for us to explain why the flow becomes unsteady and more turbulent in the experiment of $\alpha = 1\%$.

Fig. 11a shows the variation of the time constant with the intensity of cavity-bottom heating that is represented by an initial temperature difference (ΔT) between the cavity-bottom and the air. The intensity of bottom heating varies from 0°C to 10°C in 2°C intervals. The $\Delta T = 0^\circ\text{C}$ experiment means no bottom heating. The calculated bulk Richardson number (Ri_b) ranges from 0 to -1.05 for the bottom heating intensities of 0 – 10°C . Here, Ri_b is defined as follows (Uehara et al., 2000).

$$Ri_b = \frac{gH(T_{z/H=1} - T_{z/H=0})}{T_a U_{z/H=1}^2}, \quad (8)$$

where g is the gravitational acceleration, $T_{z/H=1}$ and $T_{z/H=0}$ are the averaged temperatures at the top and bottom of the cavity, respectively, T_a is the averaged temperature in the cavity, and $U_{z/H=1}$ is the averaged wind speed at the top of the cavity. The time constant decreases with increasing bottom heating intensity as a whole (Fig. 11a). The decrease of the time constant results from the increase of MKE and TKE, which is related to a coupling of thermally induced motion and mechanically induced motion (Kim and Baik, 2001), especially on the upstream side of the lower cavity.

A significant change in the time constant appears at $\Delta T = 8^\circ\text{C}$. This can be explained by a change of flow. Fig. 12 shows the time evolution of streamline at $y/H = 0$ for $\Delta T = 6$ and 10°C , with the primary vortex centers connected by a solid line. The vortex center for $\Delta T = 6^\circ\text{C}$ does not change with time (Fig. 12a), whereas the vortex center for $\Delta T = 10^\circ\text{C}$ migrates with time (Fig. 12b). As seen in Fig. 12, the flow in the cavity is in a quasi-steady state in the experiment of $\Delta T = 6^\circ\text{C}$ but is not in a quasi-steady state in the experiment of $\Delta T = 10^\circ\text{C}$. When the initial temperature difference (ΔT) exceeds a critical value (8°C in this study), the flow in the cavity becomes unsteady and strong. The increase of MKE and TKE at the critical value of ΔT reflects the change of flow. Another remarkable example of flow change by bottom heating is the meander of the core of the primary vortex in the spanwise direction. Tsai et al. (2005) showed in a three-dimensional numerical study that the vortex core meanders in an urban street canyon when the intensity of bottom heating is 5°C . Their bottom heating intensity is smaller than the critical value in the present study. When the bottom heating intensity is equal to 6°C in this study, it was found that the vortex core meanders slightly. On the other hand, the vortex core in the experiment of $\Delta T = 10^\circ\text{C}$ meanders considerably in the spanwise direction, and it also migrates with time as shown in Fig. 12b.

5. Summary and conclusions

Using a computational fluid dynamics (CFD) model, flow and dispersion in an urban cubical cavity were numerically examined. A primary vortex and secondary vortices including end-wall vortices appear in the cavity. The end-wall drag effect results in smaller average mean-flow kinetic energy in the cavity than in an urban street canyon. A trajectory analysis revealed that the end-wall vortices cause fluid particles to move in the spanwise direction.

This suggests that cubical cavity flow is essentially three-dimensional. The iso-surfaces of the Okubo–Weiss criterion capture cavity vortices well. It was found that the pollutant concentration is high near the bottom of the upstream side in the case of continuous pollutant emission and near the center of the primary vortex in the case of instantaneous pollutant emission. The time constant decreases substantially as the ambient wind speed increases. The time constant tends to decrease as the inflow turbulence intensity and cavity-bottom heating intensity increase. The time constant becomes large with oblique ambient wind direction. The high ambient wind speed was found to be the most crucial factor for ventilating the cavity. In this study, the simplest cavity geometry (say, a cubical cavity) was considered. The characteristics of flow and dispersion in a cavity can vary with different cavity aspect ratios. This needs to be investigated in a further study.

Acknowledgments

The authors are grateful to two anonymous reviewers for providing valuable comments. This work was funded by the Korea Meteorological Administration Research and Development Program under Grant CATER 2006-2202 and the Brain Korea 21 Project.

References

- Baik, J.-J., Kim, J.-J., Fernando, H.J.S., 2003. A CFD model for simulating urban flow and dispersion. *Journal of Applied Meteorology* 42, 1636–1648.
- Chiang, T.P., Hwang, R.R., Sheu, W.H., 1996. Finite volume analysis of spiral motion in a rectangular lid-driven cavity. *International Journal for Numerical Methods in Fluids* 23, 325–346.
- Freitas, C.J., Street, R.L., 1988. Non-linear transient phenomena in a complex recirculating flow: a numerical investigation. *International Journal for Numerical Methods in Fluids* 8, 769–802.
- Hall, D.J., Walker, S., Spanton, A.M., 1999. Dispersion from courtyards and other enclosed spaces. *Atmospheric Environment* 33, 1187–1203.
- Haller, G., Sapsis, D., 2008. Where do inertial particles go in fluid flows? *Physica D* 237, 573–583.
- Jordan, S.A., Ragab, S.A., 1994. On the unsteady and turbulent characteristics of the three-dimensional shear-driven cavity flow. *Journal of Fluids Engineering* 116, 439–449.
- Kim, J.-J., Baik, J.-J., 2001. Urban street-canyon flows with bottom heating. *Atmospheric Environment* 35, 3395–3404.
- Kim, J.-J., Baik, J.-J., 2003. Effects of inflow turbulence intensity on flow and pollutant dispersion in an urban street canyon. *Journal of Wind Engineering and Industrial Aerodynamics* 91, 309–329.
- Kim, J.-J., Baik, J.-J., 2004. A numerical study of the effects of ambient wind direction on flow and dispersion in urban street canyons using the RNG $k-\epsilon$ turbulence model. *Atmospheric Environment* 38, 3039–3048.
- Koseff, J.R., Street, R.L., 1984. Visualization studies of a shear driven three-dimensional recirculation flow. *Journal of Fluids Engineering* 106, 21–29.
- Lee, I.Y., Park, H.M., 1994. Parameterization of the pollutant transport and dispersion in urban street canyons. *Atmospheric Environment* 28, 2343–2349.
- Migeon, C., Pineau, G., Texier, A., 2003. Three-dimensionality development inside standard parallelepipedic lid-driven cavities at $Re = 1000$. *Journal of Fluids and Structures* 17, 717–738.
- Okubo, A., 1970. Horizontal dispersion of floatable particles in the vicinity of velocity singularities such as convergences. *Deep-Sea Research* 17, 445–454.
- Povitsky, A., 2005. Three-dimensional flow in cavity at yaw. *Nonlinear Analysis* 63, 1573–1584.
- Prasad, A.K., Koseff, J.R., 1989. Reynolds number and end-wall effects on a lid-driven cavity flow. *Physics of Fluids A* 1, 208–218.
- Shankar, P.N., Deshpande, M.D., 2000. Fluid mechanics in the driven cavity. *Annual Review of Fluid Mechanics* 32, 93–136.
- Tsai, M.Y., Chen, K.S., Wu, C.H., 2005. Three-dimensional modeling of air flow and pollutant dispersion in an urban street canyon with thermal effects. *Journal of the Air and Waste Management Association* 55, 1178–1189.
- Tsorngr, S.J., Capart, H., Lai, J.S., Young, D.L., 2006. Three-dimensional tracking of the long time trajectories of suspended particles in a lid-driven cavity flow. *Experiments in Fluids* 40, 314–328.
- Uehara, K., Murakami, S., Oikawa, S., Wakanatsu, S., 2000. Wind tunnel experiments on how thermal stratification affects flow in and above urban street canyons. *Atmospheric Environment* 34, 1553–1562.
- Versteeg, H.K., Malalasekera, W., 1995. An Introduction to Computational Fluid Dynamics: The Finite Volume Method. 198–203 and 243–244. Longman, Malaysia.
- Weiss, J., 1991. The dynamics of enstrophy transfer in two-dimensional hydrodynamics. *Physica D* 48, 273–294.